The power of computational thermochemistry in high-temperature process design and optimization: Part 1 - Unit operations

Juan-Ricardo Castillo-Sánchez[a], Kentaro Oishi[a], Laurence St-Germain[a], Dyhia Ait-Amer[a] and Jean-Philippe Harvey[a,*]

[a] *Centre for Research in Computational Thermochemistry (CRCT), Department of Chemical Engineering, Polytechnique Montréal, C.P. 6079, Succursale "Downtown", Montréal, H3C 3A7, Québec, Canada*

ARTICLE INFO

Keywords:
Computational thermochemistry
Carbo-reduction
Glass recycling
Modeling and simulation
FactSage
Pyrometallurgy

ABSTRACT

Industrial process modeling is increasingly accessible through computational chemistry packages. Computational Thermochemistry (CT) is particularly convenient for exploring the behavior of high-temperature processes (*e.g.*, pyrometallurgical unit operations such as calciners, roasters, smelters, converters, and electric arc furnaces) since their operating conditions are mostly dictated by local/global thermodynamic phase equilibria. Under these high-temperature conditions, energy barriers are small and do not limit the kinetics of many chemical reactions. In this context, engineers-in-training must take full advantage of CT to explore and understand current unit operations in high-temperature manufacturing technologies. This work illustrates the strength of computational thermochemistry for high-temperature modeling through four case studies, *i.e.*, 1. a carbo-reduction process, 2. a glass production/recycling furnace, 3. an aluminothermic reactor for the production of a ferro-niobium alloy, and 4. a titanium purification unit. Moreover, the relevance of key fundamental thermodynamic concepts is discussed through the modeling of these unit operations. All the thermodynamic simulations presented in this work were performed using FactSage, a metallurgy-specialized thermochemical package widely employed in both academia and industry.

1. Introduction

The next generation of metallurgical, materials, chemical and mechanical engineering students will face many challenges to limit the footprint of our industrial activities on earth in years to come [1, 2, 3, 4, 5, 6]. As an example, they will need to improve the sustainability of most primary and secondary industrial processes. For instance, the increasing availability of electrical work obtained from renewable energy sources provides interesting opportunities for the development of cleaner and greener pyro-metallurgical processes [7]. The primary smelting of iron via molten oxide electrolysis is a perfect example of such a potential paradigm shift in the production of commodity metals [8, 9]. The substitution of methane by green hydrogen (produced via water electrolysis [10, 11, 12]) is another path that scientists are exploring to limit CO_2 emissions. Moreover, hydrogen is seen by many as a clean energy vector (for melting furnaces or transport applications) as well as a clean reducing agent to be used for the production of metals such as iron (via Direct Reduction Iron [DRI] technologies) [13].

Process design has traditionally been tackled from multiple angles:

1. It can be approached from an experimental perspective via time-consuming and expensive trial and error lab-scale tests (ex.: development of a carbo-reduction method of manganese nodules [14]);
2. It can be inspired by existing processes which are then improved by replacing inefficient units or by adding new operation units (ex.: the addition of a combustor to the MIDREX process to improve both the heat transfer to the reducing gas as well as the efficiency of the process [15]);
3. Critical units of a process can be designed from scratch by precisely simulating their behavior using fluid mechanics and heat transfer simulation packages which often require the definition of boundary conditions (*e.g.*, selection of an optimal impeller for the mixing of solid-liquid mixtures [16]).

New design approaches based on machine learning and artificial intelligence are also being integrated in recent years into the development of new processes. Such methods require a large volume of data to train, which is often a major limitation, especially for low technology readiness level processes [17, 18, 19, 20].

Another powerful tool based on fundamental laws of physics and often overlooked is available for engineers, *i.e.* computational thermochemistry. Classical thermodynamics should always be at the heart of any process design because 1) it allows the identification of operating conditions under which targeted chemical reactions are energetically favorable; 2) it predicts both desirable and parasitic reactions required to define mass balances; 3) it provides the thermodynamic properties required to establish energy balances; 4) it defines the complex phase assemblage which is established in a multi-component system under specific constraints (which is of prime importance when selecting vessel materials in contact with the reactive systems). It also provides key ingredients in the description of reaction

*Corresponding author
juan-ricardo.castillo-sanchez@polymtl.ca (J. Castillo-Sánchez); kentaro.oishi@polymtl.ca (K. Oishi); laurence-1.st-germain@polymtl.ca (L. St-Germain); ait-amer.dyhia@polymtl.ca (D. Ait-Amer); jean-philippe.harvey@polymtl.ca (J. Harvey)
ORCID(s): 0000-0002-7479-7580 (J. Castillo-Sánchez); 0000-0001-5367-6619 (K. Oishi); 0000-0001-8572-7767 (J. Harvey)

kinetics since chemical potentials are the driving force for diffusion. Also, the activity (also called affinity) of a phase defines the energetic driving force for its formation. Chemical potentials can be imposed when performing equilibrium calculations (instead of mass balances) to track the phase assemblage as a function of their temporal evolution. The kinetic modeling challenge is then to describe the temporal evolution of these chemical potentials. The use of high-temperature processes and highly reactive systems tipically increase the risk of undesired and uncontrolled reactions, including fire hazards and explosions. These numerous challenges render a trial-and-error approach virtually unfeasible for most high-temperature pyrometallurgical processes.

Consequently, computational thermochemistry should be a critical discipline at the heart of the academic curriculum of engineers. It is particularly useful for high-temperature applications (where local/global equilibrium states can be reached as thermally activated processes are favored) [21] and for systems that are more difficult to probe and instrumentalize (such as high-temperature pyrometallurgical reactors). Herein, the modeling of such high-temperature technologies is illustrated through individual unit operations (Part 1). Other examples of effective applications of CT for advanced process modeling techniques include: (i) interlinked local equilibria in flow charts or transformation units [22, 23], and (ii) the linkage between localized equilibria and computational fluid dynamics (CFD) simulations [24, 25, 26]. Future research endeavors will investigate advanced process modeling (Part 2) aiming to reproduce multiple unit operation junctions (process flow charts).

This work (Part 1) aims to explore different computational thermochemistry simulations performed *via* the FactSage software [27] linked to the design of pyro-metallurgical unit operations (specifically under the assumption of closed system behavior). These examples (which can be simply set up and run from the software interface) demonstrate how the feed chemistry of raw materials and the final product specifications can be accounted for during a process design *via* computational thermochemistry. The optimum operating conditions defined in our simulations are then compared with available data from the literature to confirm their accuracy.

2. FactSage: A computational thermochemistry package for process design

In a nutshell, computational thermochemistry consists of building mathematical functions that describe the Gibbs free energy of each phase that may form in a system. These functions are called thermodynamic models and are tailored for each phase. The parameterization of each Gibbs free energy function using available experimental and numerical data (also called the CALPHAD approach) enables the evaluation of a system's phase assemblage under specific imposed equilibrium conditions. The fundamentals of the CALPHAD approach and the principles of Gibbs free energy minimization (phase assemblage determination) can be found in the work of Pelton [28], Saunders & Miodownik [29], Lukas *et al.*[30] and Harvey *et al.* [31]. Computational thermodynamic packages such as FactSage integrate all these ingredients so that a user can predict the equilibrium state for a wide range of complex chemical systems containing metals and alloys, oxides, salts and more [32].

The main FactSage interface used to perform the equilibrium calculations presented in this work (called the *Equilib* module) is shown in Figure 1. The first step to perform an equilibrium calculation is to select the adequate thermodynamic database. In FactSage, there are more than 25 specialized databases for the energetic description of oxides, sulfides, carbides, molten salts, and alloys. The different reactants and their respective quantities are then defined in the interface. At this point, there is the option of defining (or not) the initial state of each reactant. The evaluation of the variations of state properties of the system (such as the variation of enthalpy to perform energy balances) requires the definition of the initial conditions, while the analysis of the phase assemblage which occurs in the system does not require them.

The next steps are to select the potential phases that may form in the system and define the imposed equilibrium conditions for the calculations. It is possible to define a phase as dormant. In this case, the dormant phase does not appear in the phase assemblage, but its activity is evaluated. This strategy is used when one wants to explore meta-stable phase equilibria or to evaluate the energetic driving force for the formation of a specific phase. Finally, the equilibrium calculation is performed using the SOLGASMIX algorithm [33, 34, 35, 36], and the results can be analyzed and presented as figures.

3. Design of high-temperature pyro-metallurgical unit operations using computational thermochemistry

Metals and alloys are used in almost all technologies surrounding us: *i.e.*, in buildings, cars, airplanes, bikes, household appliances, electronics, sports equipment, and many others [37], because of their stunning specific mechanical and physical properties. Unfortunately, most of these metals are not available in their native state in the earth's crust and are generally oxidized and chemically bonded to oxygen (oxide), sulfur (sulfide), phosphorus (phosphides), or other complex anions (carbonate, sulfate, etc.). In pyrometallurgy, these valuable minerals embedded in a wide variety of ores (which also contain unwanted gangue) are the traditional raw materials used in the primary production of metals. Those minerals are refined at high temperatures in different pyro-metallurgical processes, often in the presence of liquid phases, to extract the desired metals or other intermediate compounds that may require further refining

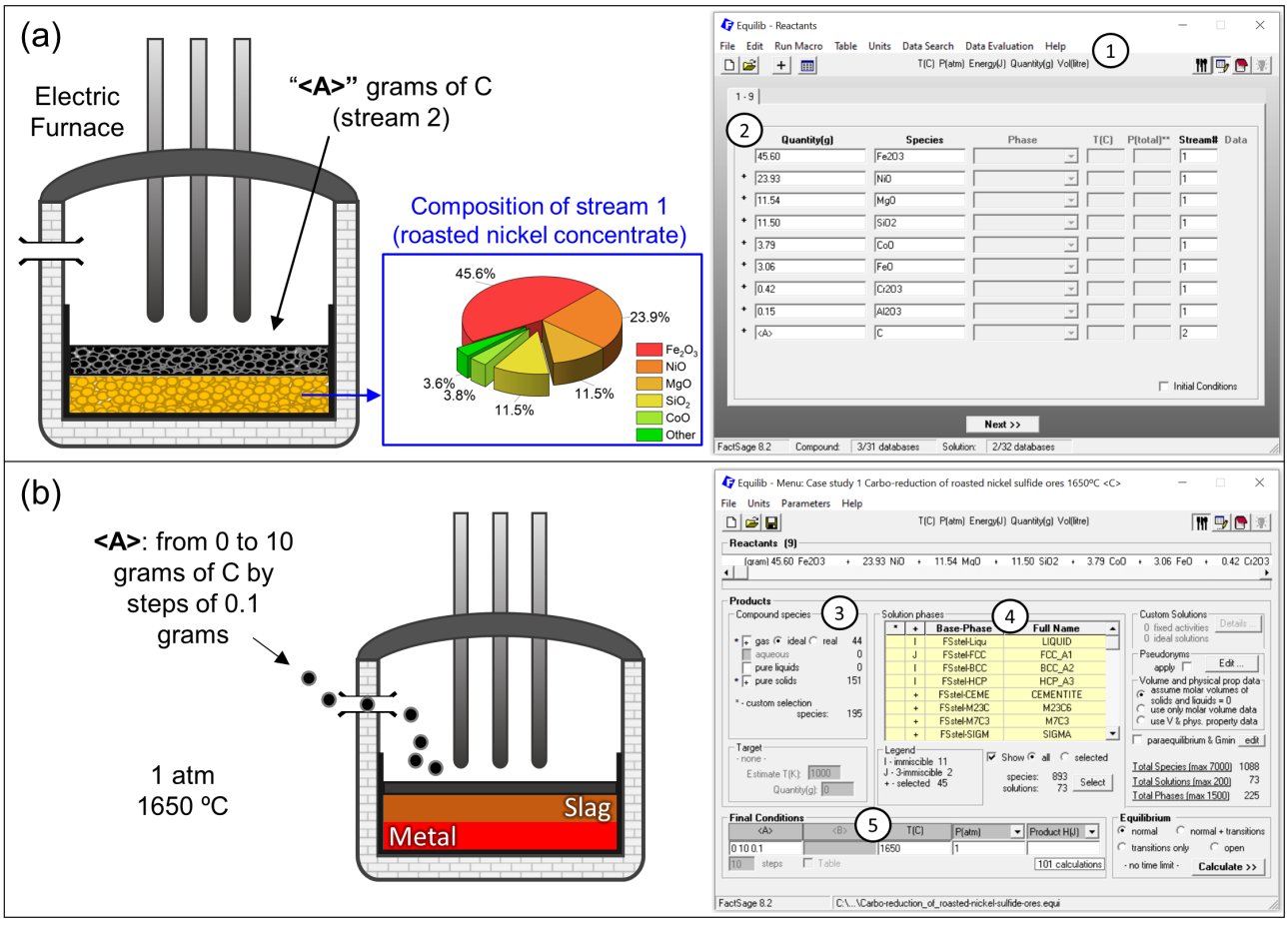

Figure 1: *Equilib* module main screens (example for the carbo-reduction of roasted nickel concentrate): 1) Ribbon tabs; 2) reactants' specification panel; 3) Compound species panel; 4) Solution phases section; 5) Operating/equilibrium conditions panel. A graphical representation of the roasted nickel concentrate reduction is provided on the left side for the reactants section (a) and for the operating/equilibrium conditions section (b). The inputs provided in this figure were used to generate the simulation results of section 3.1.1.

[38]. Nowadays, engineers and scientists also need to account for high volumes of scrap and obsolete technological equipment which contain high levels of valuable metals. The scrap can be almost fully compatible with traditional primary processes (such as iron) or may need dedicated secondary processing technologies (such as for aluminum with re-melting furnaces) to obtain the desired metal. Refining challenges also often occur when dealing with scrap, such as the unwanted presence of copper in iron scrap, which is challenging to remove [39, 40, 41, 42, 43, 44, 45, 46]

There are many unit operations in pyrometallurgy. Roasting is often used to transform sulfide minerals difficult to process, such as sphalerite (ZnS) into an oxide compound for which the valuable metal is easier to extract, *e.g.*, ZnO, which can be dissolved in an acidic solution and then electrowinned to ultimately produce Zn [47]. Oxygen-enriched air is typically injected into a rotary furnace to achieve this task. Calcining is another frequent unit operation used to prepare a concentrate for smelting operations. Carbonates and hydrates are often calcined to remove CO_2 and H_2O from their structures, resulting in the formation of oxides [48]. Calcining requires energy as it is typically an endothermic reaction. Reduction and oxidation operations are almost always integrated with pyro-metallurgical operations [49]. Reduction using carbon allows the elimination of oxygen from the system while air (or O_2-enriched air) injection allows the oxidation of impurities, which are then transferred to a slag phase or an exhaust gas. Apart from these two cheap reactants (*i.e.*, carbon and air), other chemicals used as flux and precipitating agents can be added to purify and refine metals. In this case, physical separation operations are required; for instance, slag tapping [50] and liquid metal filtration [51]. Finally, other unit operations such as distillation, zone melting refining, electrowinning and electrorefining can be added to pyrometallurgical processes to meet the final specifications of the desired product.

In this context, computational thermochemistry can be used to (1) define reducing conditions of complex oxide-based concentrates, (2) solve overall mass and energy balances for a given feed by simultaneously considering all possible reactions (both desired and parasitic reactions) that may occur in a given pyrometallurgical unit operation, (3)

evaluate partition coefficient of critical elements in the different phases which are in equilibrium, (4) quantify the vapor pressure of volatile elements and more.

3.1. Case study #1: Carbo-reduction - going beyond the Ellingham diagram

The first necessary condition in the design of a process is to obtain favorable energetics for the main targeted reaction to occur. This criterion is quantified by the variation of the Gibbs free energy of this specific chemical reaction. Here is an example of such a chemical reaction for the carbo-reduction of hematite by coke:

$$2Fe_2O_3(s) + 3C(s) \rightarrow 3CO_2(g) + 4Fe(s) \quad (1)$$

with

$$\Delta G(T,P) = \Delta G^\circ + RT \cdot ln\left[\frac{P^3_{CO_2} \cdot a^4_{Fe(s)}}{a^2_{Fe_2O_3(s)} \cdot a^3_{C(s)}}\right] \quad (2)$$

Reaction 1 will proceed to the right if the variation of its Gibbs free energy, *i.e.*, ΔG defined in eq.2, is negative. The evaluation of this thermodynamic criterion requires the knowledge of the standard Gibbs free energy of this reaction (ΔG°) as well as the definition of the activity a_i of each reactant and product. Moreover, it is often assumed in pyrometallurgy that gaseous species form an ideal gas solution. In this case, their fugacity can be approximated by their partial pressure P_i.

When dealing with standard conditions, well-known graphical tools such as Ellingham diagrams [52] can be used to rapidly identify favorable conditions for carbo-reduction (*i.e.*, eq. 1), roasting or calcining operations. An example of such a diagram is presented in Figure A.1. This diagram is essentially the plot of the Gibbs free energy of the formation of a series of oxides (*i.e.*, the thermodynamic driving force that predicts if a reaction can occur) as a function of temperature on a 1 mol basis of O_2:

$$\frac{4}{\nu}M(s,l,g) + O_2(g) \rightarrow \frac{4}{\nu}MO_{\frac{\nu}{2}}(s,l,g);\ \Delta G^\circ \quad (3)$$

Assuming $\Delta C_P \approx 0$ for reaction 3, the following approximation is obtained:

$$\Delta G^\circ_i(T, 1\text{atm}) \approx \Delta H^\circ_i - T\Delta S^\circ_i = \alpha_i + \beta_i T \quad (4)$$

The extrapolated intercept of each curve at 0K corresponds to the value of ΔH°_i while the slope β_i defines ΔS°_i. A negative value for ΔH°_i indicates that the oxidation reactions that lead to the formation of these oxides are all exothermic. Oxides at the top of the diagram are the least thermodynamically stable, while those at the bottom have the highest affinity to oxygen and are highly stable. Slope changes of these curves are due to phase transformations of either reactants or products. It is important to mention that the linear approximation of ΔG°_i (eq. 4) represents a limitation for practical applications, as it does not fully capture the temperature dependence of thermodynamic properties. Contrary to that, CT packages are equipped with meticulously calibrated temperature-dependent heat-capacity data. Hence CT allows for a reliable description of state properties, which is particularly valuable for achieving accurate mass and energy balances.

As seen in Figure A.1, most slopes associated with the formation of oxides are positive as the entropy of condensed phases (liquid and solid) is smaller than that of gaseous species [53], which leads to negative entropy of formation. A careful analysis of the Ellingham diagram for oxides shows the two exceptions to this slope trend, the formation of CO_2 and CO. For CO_2, the slope is practically a horizontal line since the entropy contributions are mainly affected by the gas phase (in this case, 1 mol of gas of reactants produces 1 mol of gas). For CO, the number of moles of gas produced is larger than the number of moles of gas in the reactants, which results in a positive entropy of formation (or equivalently negative slope in the Ellingham diagram). Because of this attribute, carbon is a key reactant for the reduction of many metal oxides (which is called carbo-reduction). It is also a relatively cheap reactant (in the coke form [54]) and releases a substantial amount of energy when oxidized. This release of energy can be advantageously collected to heat the system.

By using the diagram Ellingham (Figure A.1), it is theoretically possible to define the temperature above which each metal oxide can be reduced by carbon under standard conditions. This temperature is defined by the intercept between the Gibbs free energy of formation of a given oxide and the one of CO(g) (or equivalently CO_2). It is also possible to evaluate the oxygen partial pressure P_{O_2} required to reduce an oxide at a given temperature under non-standard conditions. To do so, a straight line that starts at the O point on the 0K y-axis is plotted. This line intercepts the Gibbs free energy of the oxide at the targeted temperature. The required P_{O_2} for this reduction is obtained by extending the straight line up to the $log_{10}(P_{O_2})$ scale on the right-hand side of the diagram. The use of the Ellingham diagram as a graphical tool to define real-life operating conditions for the reduction of metal oxides is limited for the following reasons: (1) it assumes that reactants and products are pure compounds (no solid or liquid solutions are considered), (2) it assumes that reactants and products are in equilibrium, and (3) it does not report all the other possible chemical reactions that can occur in the system. Thermodynamic simulations of the carbo-reduction of complex oxides systems performed using the FactSage software (which allows the description of many solid and liquid oxide and metallic solutions) circumvent all these limitations.

3.1.1. Carbo-reduction of roasted nickel sulfide ores

The ferronickel production through the roasting and carbo-reduction of nickel sulfide ores will be used in this section to demonstrate the strength of the computational thermochemistry approach to simulate this process. Ferronickel, containing 19-38%(wt.) Ni, is mainly dedicated

Table 1
The elemental composition of the nickel concentrate obtained from the mineralogy of the sulfide concentrate and the oxide composition of the roasted nickel concentrate.

Concentrate		Calcine	
Component	Composition wt. %	Component	Composition wt. %
Ni	17.39	Fe_2O_3	45.60
Cu	0.20	NiO	23.93
Fe	31.70	MgO	11.54
S	15.82	SiO_2	11.50
Mg	6.44	CoO	3.79
Si	4.81	FeO	3.06
Al	0.07	Cr_2O_3	0.42
Cr	0.26	Al_2O_3	0.15
Co	2.76		

to the production of stainless and heat-resistant steels [55]. In 2005, ferronickel produced from laterite ores accounted for 30% of worldwide primary nickel production [56]. Its production usually involves two steps: (1) calcination of laterite ores in a rotary kiln and (2) calcine smelting in an electric furnace [55, 57, 58]. Nickel sulfide ores are typically converted into matte and are thus usually not used to produce ferronickel [57, 58].

When dealing with low-sulfur-and-copper-bearing Ni sulfide concentrates, the ferronickel route can also be a viable option. Typically, Ni sulfide concentrate has the following composition (wt.): 10% Ni, 2% Cu, 40% Fe, and 30% S [59]. The low-grade Ni concentrate that was considered in this section contains about 17% Ni, 0.2% Cu, 30% Fe and 16% S, as shown in Table 1. This composition was estimated by converting the mineral composition of the sulfide concentrate into an elemental composition.

Ferronickel production from this concentrate can be carried out in two stages: first, the concentrate is industrially roasted at ∼700 °C [58] in a fluidized bed roaster to oxidize the Ni/Fe-rich sulfide ore, culminating in a complex oxide mixture (Table 1). The resulting calcine is then treated through a carbo-reduction process at a temperature of about 1550-1650 °C [60] in an electric furnace (Figure 1). This operation reduces nickel and iron oxides and generates a ferronickel alloy containing more than 50% Ni. Most impurities (*i.e.*, Co, Si, P, S) are transferred to the slag for disposal. To simplify the calculations, smelting simulations of this section were performed under isothermal conditions at 1650 °C. Electric furnaces used in industrial processes often operate at constant pressure, hence a fixed pressure of 1 am was considered for this simulation.

The chemical composition of the calcine used in the carbo-reduction simulations is presented in Table 1. The thermodynamic simulations of the carbo-reduction consist of injecting an $\langle A \rangle$ amount (in grams) of carbon into this calcine feed (using a 100-gram of calcine basis, as shown in Figure 1). The use of $\langle A \rangle$ parameter in this simulation allows to delve deeper into the extraction mechanism by approximating the reduction stages to the equilibrium at different C additions. This assumption entails that all C is presumed to react fully with the ore, with the exception of cases involving an excess of C where it might appear as a stoichiometric compound in the final phase assemblage. This approximation enables to mimic the non-iso-compositional behavior of the feedstock (oxide-based phases) and the desired product (metallic alloy) across the reduction stages, *i.e.*, the evolution of the oxide from the raw materials (solid and liquid phases at high-T) and that of the metal of interest (potentially as a molten metal phase at high-T) can be monitored. The overall system was considered iso-compositional given the low volatility of Fe and Ni in the alloy of interest. The databases selected for this simulation are FToxid (for the oxide-based solutions), FactPS (for the gas phase and stoichiometric compounds), and FSstel (which is an optimized database for the steel industry). For the given calcine composition (Table 1), multiple solid oxide phases are relevant for the smelting modeling, including the monoxide and spinel. At high temperatures, the slag phase for the molten oxide and the molten metal phase should be considered as well. In some cases, additional components appear depending on their thermal stability, such as intermetallics, disorder phases, carbides, etc. Beginner and intermediate FactSage users are encouraged to select all the models available for their systems of interest. On the other side, expert users can optimize their phase selection to speed up the calculations. For the *equi* file of this example (Supplementary Material), all gaseous species, solid compounds and solution phases were included.

At an operating temperature of 1650 °C and a pressure of 1 atm, the phase assemblage that occurs as a function of carbon addition is presented in Figure 2(a). At the early stage of the carbo-reduction process (*i.e.*, between 0 and 1 g of carbon), no liquid metal is produced. Therefore, the carbon is preferentially used to reduce Fe_2O_3 to FeO, which are both found in the slag and monoxide phases. A Fe_3O_4-$FeNi_2O_4$ spinel also forms in a narrow range of carbon addition and is reduced very quickly. At 1.5 g of carbon, the liquid metal phase appears, and carbon starts reducing NiO, CoO and FeO to their metallic state, which transfer to the liquid metal solution as shown in Figure 2(a)-(b). Virtually all silicon and magnesium will remain in the slag in the form of oxides (Figure 2c). By analyzing the metal composition in Figure 2(b), it is possible to predict how much carbon is required to reach the targeted ferronickel quality (55-60 wt.% Ni) *i.e.*, between 7.5 to 8 g of carbon per 100 g of calcine. This carbon addition maximizes the transfer of Ni from the slag (Figure 2c) to the ferronickel alloy (Figure 2b). The unconsumed Fe, Si and Mg from the feedstock remain in the slag phase (Figure 2c at 8 g of C/100 g of calcine). When adding less than 2.6 g of carbon, a Fe_2O_3-FeO-NiO monoxide will form, which can be fluxed by adding about 2.5g of SiO_2/100 g of feed (Figure 3). The addition of SiO_2 as a flux agent is a common strategy employed in pyrometallurgy to promote slag formation. Apart from their high melting points, ferronickel slags in electric furnaces are known for their strong acid character, which is detrimental

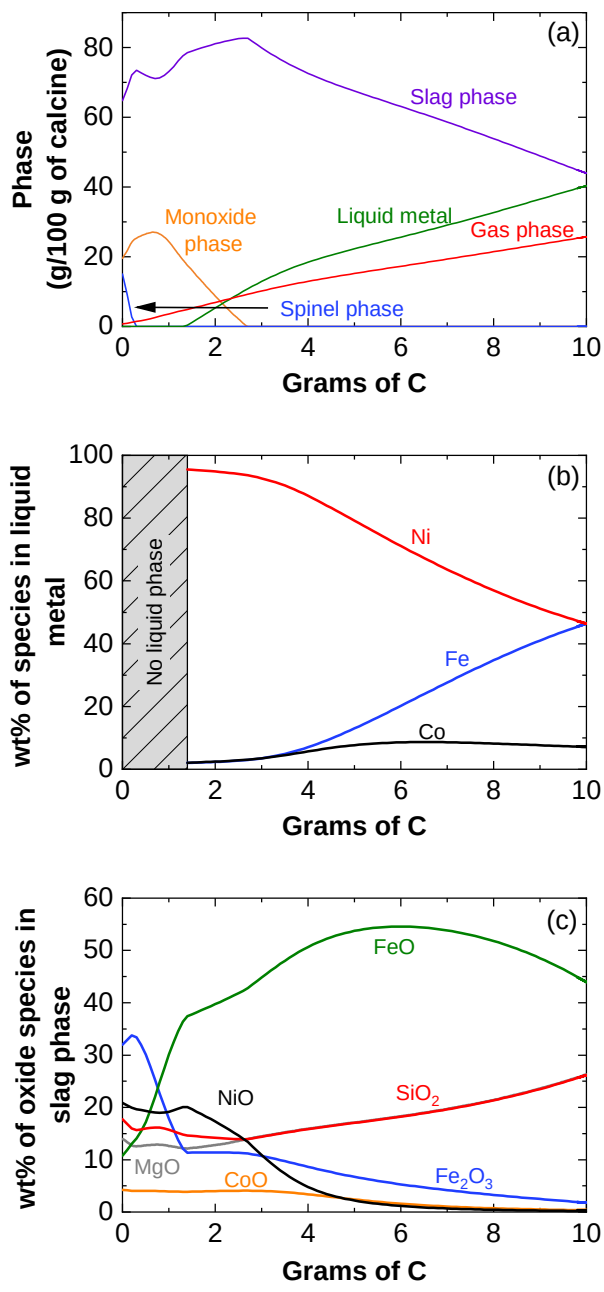

Figure 2: Calculations results for the carbo-reduction of the roasted nickel sulfide concentrate: (a) amount (in g) of equilibrium phases generated as a function of carbon addition (in g); (b) elemental composition (wt.%) of the liquid metal. Shaded gray represents the zone where the liquid phase is not stable; (c) oxide species (wt.%) in the slag phase.

to the furnace lifespan [61]. To control corrosion, lining materials such as magnesia are effectively used for ferronickel production [61]. Therefore, the global mass balance from CT simulations may differ from real operations as a result of the slag/refractory interactions.

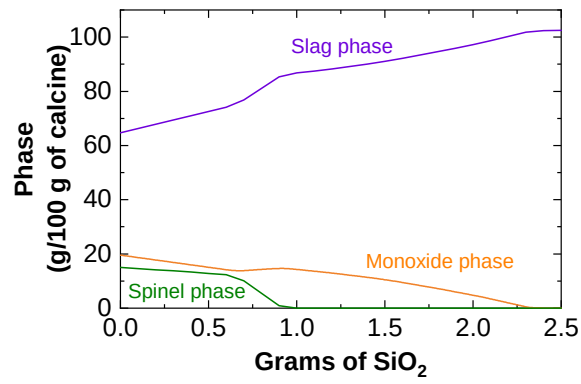

Figure 3: Evolution of the phase assemblage as a function of SiO_2 additions into 100 of calcine at 1650°C.

3.2. Case study #2: Energy and mass balances for glass production and recycling

Soda-lime glasses are widely employed for packaging applications [62]. Glass containers are typically manufactured using natural gas melting furnaces, followed by a press-blow forming process [63]. The latter involves blowing molten glass within molds to create bottles or other specific-shaped glass packages. A typical soda-lime glass composition is presented in Table 2. Conventional reactants to produce this material are mainly silica and carbonates (Table 2). Alkali and alkaline-earth oxides are commonly introduced in the batch as carbonates, such as soda ash (Na_2CO_3), potash (K_2CO_3), and limestone ($CaCO_3$). Double-carbonate minerals, *e.g.*, dolomite ($[1\text{-}x]CaCO_3 \cdot xMgCO_3$), can also be employed in glass production. In order to increase the chemical resistance, alumina (Al_2O_3) is commonly added as an intermediate oxide. It can be added as pure alumina or alumina hydrate ($Al_2O_3 \cdot 3H_2O$); therefore, no CO_2 is released [64].

Upon heating, some carbonates are thermally decomposed to form oxides and release CO_2. In their pure state, anhydrous alkali Na_2CO_3 and K_2CO_3 carbonates are stable at high temperatures and have melting points of 851°C and 891°C, respectively [66]. For Na_2CO_3, its decomposition is only noticeable above the melting point [67]. Yet, it is possible to thermally decompose those carbonates (releasing CO_2) at lower temperature when they are combined with other glass ingredients (silica-rich mixture as shown in Table 2). For this example, the feedstock is entered as individual reactants into FactSage (*equi* files in Supplementary Material), according to the mass balance of Table 2. By activating the "`Initial conditions`" option (bottom-right option of the main *Equilib* module Figure 3.1.1a), FactSage will automatically indicate the stable allotropes for the specified conditions. This option enables the calculation of state property changes. Herein, the enthalpy change is particularly useful to estimate the energy demands for the glass furnace. The molten glass of interest consists of a liquid oxide solution; therefore, it can be described with the slag phase solution model. Multiple solid oxides-based

Table 2
Chemical composition of a typical soda-lime glass (left side) and the direct CO_2 emissions associated with reactants to produce 1 kg of soda-lime-silica glass (right side).

Component	Composition	Reactants	Amount	Emissions CO_2	
				Extraction	*Decomposition*
	(wt. %)		(kg)	(kg CO_2)	(kg CO_2)
SiO_2	73.6	Silica (sand)	0.7360	0.02439[a]	-
Na_2O	16.0	Na_2CO_3	0.2736	0.31342[a]	0.1136
CaO	5.2	$CaCO_3$	0.0928	0.00772[a*]	0.0408
MgO	3.6	$MgCO_3$	0.0753	0.00626[a*]	0.0393
Al_2O_3	1.0	Al_2O_3	0.0100	0.01414[a]	-
K_2O	0.6	K_2CO_3	0.0070	0.00027[a]	0.0022
		Total CO_2	-	**0.3662**	**0.1959**

[a]Estimations obtained using the IMPACT 2002+ method with the Cutoff system model, employing the Ecoinvent 3.9.1 database [65].
*CO_2 emissions from $CaCO_3$ and $MgCO_3$ were obtained from dolomite production in Ecoinvent 3.9.1 database.

and carbonate-based compounds/solutions appear during the multi-phase assemblage evolution upon heating; however, it is rather easier to infer the thermal decomposition through the CO_2 emissions in the gas phase. In the same manner as in case study #1 (Section 3.1.1), it is recommended to select all the compounds and phases. Simulations were performed between 25 and 1600 ºC. Glass furnace units do not require drastic vacuum conditions; therefore, calculations were performed under isobaric conditions at 1 atm. Mandal *et al.* [68] studied the volatility of glass components varying the melting time from 30 min to 3 h; they reported the B_2O_3 as the most volatile species followed by K_2O. The glass composition requirements for this work do not include B_2O_3 and only a small amount of K_2O. Therefore, the overall system was considered iso-compositional.

The evolution of CO_2 release linked to the thermal decomposition of carbonates mixed with silicon dioxide (reactants in Table 2) is presented by the red line in Figure 4. It can be observed that all carbonates have thermally decomposed after heating up to 300 ºC. The CO_2 release at this stage accounts for 0.1959 kg/kg of glass. This amount perfectly matches the total CO_2 emissions reported in Table 2, which was obtained considering the individual decomposition of carbonates using the following relationship: $\Sigma[M(CO_2)/M(\text{carbonate } i) \times (\text{mass of carbonate } i \text{ per kg of glass})]$, where M denotes the molar mass.

Once the thermal decomposition takes place (around 300 ºC in Figure 4), the mixture of oxides is melted and heated up to 1600 ºC. According to Figure 4, oxides start melting at around 620 ºC (green Slag phase #1 line). At 1600 ºC, the oxides are contained in a monophasic system; this plot also ensures that 1kg of molten glass (Slag phase) is produced at 1600 ºC considering the initial mass balance of Table 2. Hence, at 1600 ºC all the feedstock has been transformed. In terms of materials compatibility, alumina is widely employed as a refractory material in the glass industry due to its remarkable corrosion resistance [69]. As indicated in Table 2, alumina is an essential component in

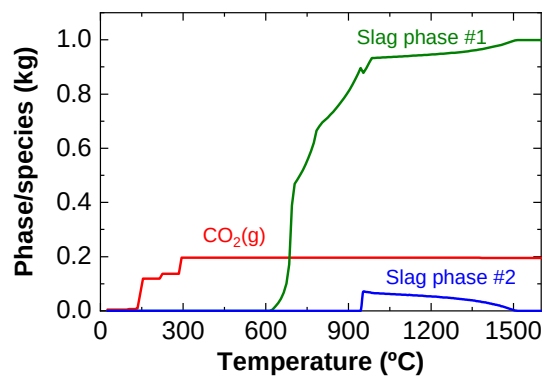

Figure 4: Evolution of CO_2 and slag phases (molten oxides) as a function of temperature.

the desired composition of the final glass. Therefore, alumina contamination may not be necessarily harmful during the slag preparation, but it should be carefully monitored to meet the desired product specifications.

The theoretical energy requirements (calculated using the FactSage software and databases) to produce 1 kg of such a primary glass from carbonates are presented in Table 3. The overall energy balance for the production of molten glass contains two main contributions: (1) the energy requirement for thermal decomposition of the carbonates (endothermic reactions), which is +0.635 MJ per kg of produced glass. The exothermic reaction associated with the mixing of the individual components from 25°C to 300°C is also accounted for in this contribution. (2) the energy requirement for heating and melting the oxide components, which is +2.340 MJ per kg of glass in this example. According to the thermodynamic calculations, a total of +2.975 MJ is required to produce 1 kg of glass. For a furnace that uses 50 % of cullets (*i.e.*, crushed recycled glass), this energy requirement drops to +2.627 MJ/kg since less energy is required for the thermal decomposition of the carbonates (heating and melting of recycled glass from 25ºC to 1600ºC

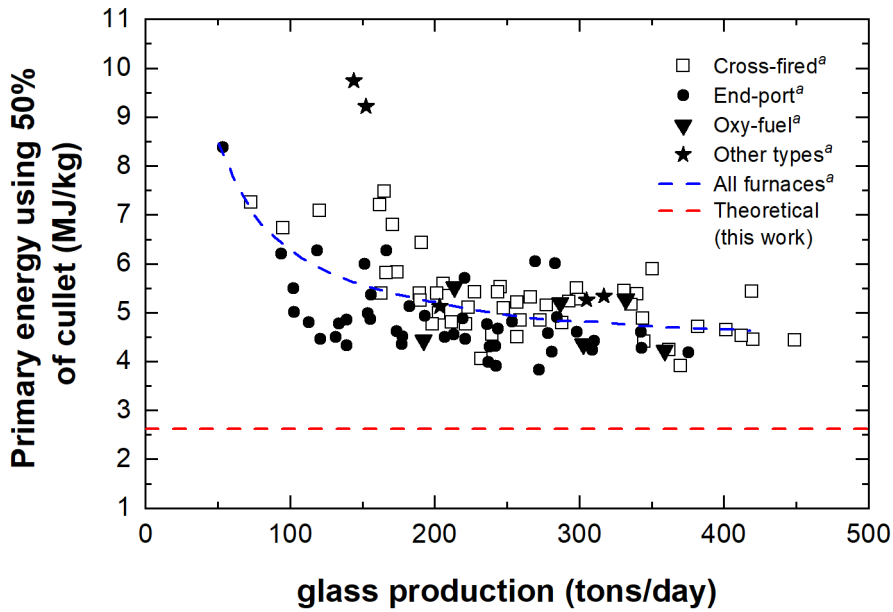

Figure 5: Energy requirement (MJ/kg) for the production of common glass as of function the furnace capacity (tons/day) for different furnace technologies [70][a] with permission obtained from the publisher. The red dashed line stands for the simulation results obtained in this work.

Table 3
Theoretical energy requirements for the production of 1kg of primary glass at $T_{furnace}$=1600°C. The combustion of the Air/Natural gas mixture (ratio 10.1:1, respectively) produces 0.2755 kg of CO_2/MJ of energy.

Contribution	Energy (MJ per kg of glass)	Direct CO_2 emissions ([Air]:[Natural gas] ratio of 10.11:1) (kg)
Thermal decomposition (25 to 300°C)	+0.635	0.1750
Heating and melting (300 to 1600°C)	+2.340	0.6447
Total	**+2.975**	**0.8197**

accounts for +2.280 MJ/kg of glass). This theoretical value is to be compared with the compilation of actual operation data presented in Figure 5. This figure shows that the thermal inertia of larger furnaces lowers energy consumption. In addition, the calculated theoretical energy requirements and the thermal efficiency of a high-performance 300 tons-per-day melting furnace (≈ +4.8 MJ per kg of glass) is about 54.7 %, which compares well with the furnace efficiencies reported in the literature.

Another valuable piece of information that can be calculated from computational thermochemistry is the amount of direct CO_2 emissions released from the natural gas combustion used to meet the energy requirements of the process.

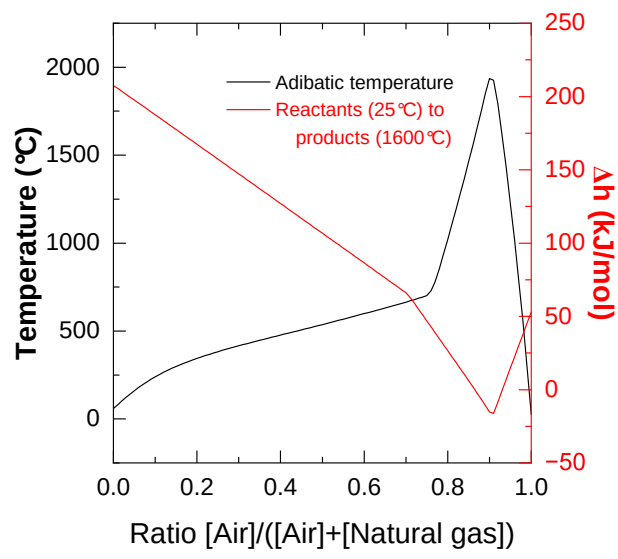

Figure 6: Adiabatic temperature (red line) and changes in enthalpy (red line) as a function of the [Air]:[Natural gas] ratio for combustion.

Figure 6 shows the evolution of the adiabatic flame temperature (black line) and the evolution of the heat requirement/release upon combustion of natural gas at 1600°C (red line) as a function of the air molar fraction in the system. Air was considered as a 78.084% N_2, 20.946% O_2 and 0.934% CO_2, while the natural gas stream is made up of 94.7%

CH_4, 4.2% C_2H_6, 0.2% C_3H_8 and 0.04% C_4H_{10}. According to this figure, an optimal [Air]:[Natural gas] molar ratio of 10.11:1 or 0.91 [Air]/([Air]+[Natural gas]) maximizes the adiabatic temperature, as well as the heat release at 1600°C. The identification of this optimal [Air]:[Natural gas] combustion ratio and associated heat release ultimately allows the quantification of the CO_2 emissions as presented in Table 3. These direct CO_2 emissions can be combined with the ones associated with the extraction of the raw materials (obtained using the Ecoinvent database [65] in OpenLCA) and to the thermal decomposition of carbonates which are presented in Table 2. The system boundaries for the quantification of CO_2 emissions are presented by the dashed line in Figure 7. The production of 1kg of glass cullet is reported to emit 0.01437 kg of CO_2 emissions (estimated employing the IMPACT 2002+ method with the Cutoff system model, using the Ecoinvent 3.9.1 database [65]). This set of data allows the definition of the theoretical CO_2 emissions upon the production of 1 kg of glass which can be expressed as follows:

$$kg\ CO_2 = (1-\alpha)\cdot(0.3662+0.1959)+\alpha\cdot 0.01437 + (\frac{1}{\eta})\cdot(1-\xi)\cdot[0.8197\cdot(1-\alpha)+0.6282\cdot\alpha] \quad (5)$$

In this equation, α is the weight fraction of cullets used in the production of the glass, η is the thermal efficiency of the melting furnace and ξ is the fraction of renewable energy (which replaces natural gas) used to heat the furnace. According to this equation, it is possible to reduce the direct CO_2 emissions by exclusively melting cullets ($\alpha = 1$ in Figure 8) and by fully replacing natural gas with green hydrogen, for example as an alternative fuel in the furnace ($\xi = 1$, purple line in Figure 8). Note that the CO_2 emissions linked to the production of natural gas or renewable energies were not considered for this work (Figure 7).

3.3. Case study #3: Elemental partitioning in a classical aluminothermic reactor to produce niobium

The prediction of the partition coefficient of the various elements constituting a given concentrate when operating a pyro-metallurgical process is at the heart of an efficient metal extraction strategy. It quantifies the efficiency of the process to remove impurities from the desired metal. The chemical specifications of the final product are defined by its applications. As an example, ultrahigh-purity copper (UHPC) requires a 99.999 wt.% purity when used for electrical applications [71]. On the other hand, carbon and oxygen concentrations (expressed in ppm by weight) in stainless steel are tightly controlled to avoid carbide and oxide inclusion formation during the elaboration process. This section explores the partition coefficient of different elements during the production of niobium, which is an important alloying element in steel.

Niobium is a refractory metal with a significantly high melting point of 2468°C [72]. The steel industry consumes about 85-90% of the total niobium output in the form of iron-niobium master alloys (ferroniobium). It is highly valued in steel for its anti-corrosion and strengthening properties [73]. For instance, niobium-bearing high-strength low-alloy (HSLA) steels are used in cars, pipelines and heavy infrastructures [73]. Niobium is also used in the production of (1) niobium-zirconium alloys for the nuclear industry (these alloys have a low neutron capture cross-section) and (2) heat-resistant superalloys found in gas turbine components (in which niobium is introduced in the form of nickel-niobium or cobalt-niobium [73]). The primary source of niobium is pyrochlore, a mineral that appears in carbonatite complexes with the theoretical formula $(Ca,Na)_{2-m}Nb_2O_6(O,OH,F)_{1-n}xH_2O$, where Na and Ca can be replaced by Ba, Sr, rare earth elements or radioactive elements [73]. More than 90% of the world's niobium production comes from the ore of the CBMM mining company located in Araxá (Brazil) [74]. It contains about 2.5% Nb_2O_5 as well as lead, rare earth (cerium and lanthanum) and radioactive (thorium and uranium) impurities [75]. To eliminate impurities in the form of gangue, the ore must undergo a series of processing stages. These stages include various physical and chemical methods, which are designed to separate the valuable components of the ore from the gangue minerals. The following is an overview of some typical processing stages that may be involved: (1) crushing, (2) ball-mill grinding, (3) magnetic separation, (4) desliming, and (5) froth flotation [76]. At this stage, the flotation concentrate still contains high levels of phosphorous, lead, and sulfur [76]. Those impurities can be removed via leaching or carbo-reduction [77].

Leached concentrate mostly contains oxides and can be reduced to metallic Nb via an aluminothermic process. The normalized average composition of the CBMM leached concentrate [76] used in our thermodynamic simulations is provided in Table 4. For the sake of simplicity, water and U_3O_8 (which are typically present in the concentrate in trace amounts) are removed from the feed since they do not significantly impact the results of our simulations. For an aluminothermic process operating at 2400 °C, iron and niobium from the concentrate are reduced and form a molten metal solution.

As a result of this operation, a standard-grade ferroniobium (≈ 60% Nb) dedicated to steel industry applications is produced. The impurities are mostly transferred to the slag for their disposal. There exist different technologies available to perform this high-temperature operation, such as electric arc furnaces and batch aluminothermic reactors [72]. The thermodynamic simulation of this process is based on a batch aluminothermic reactor (as operated by CBMM [76]). Firstly, each charge is mixed with aluminum powder, lime and fluorspar (which act as fluxing agents) as well as hematite (which is used to increase the iron content in the final ferroniobium product). Additions of hematite also provide heat to the reactor upon its reduction. This heat release allows maintaining the high operating temperature of the reactor, thus ensuring good slag-metal separation as

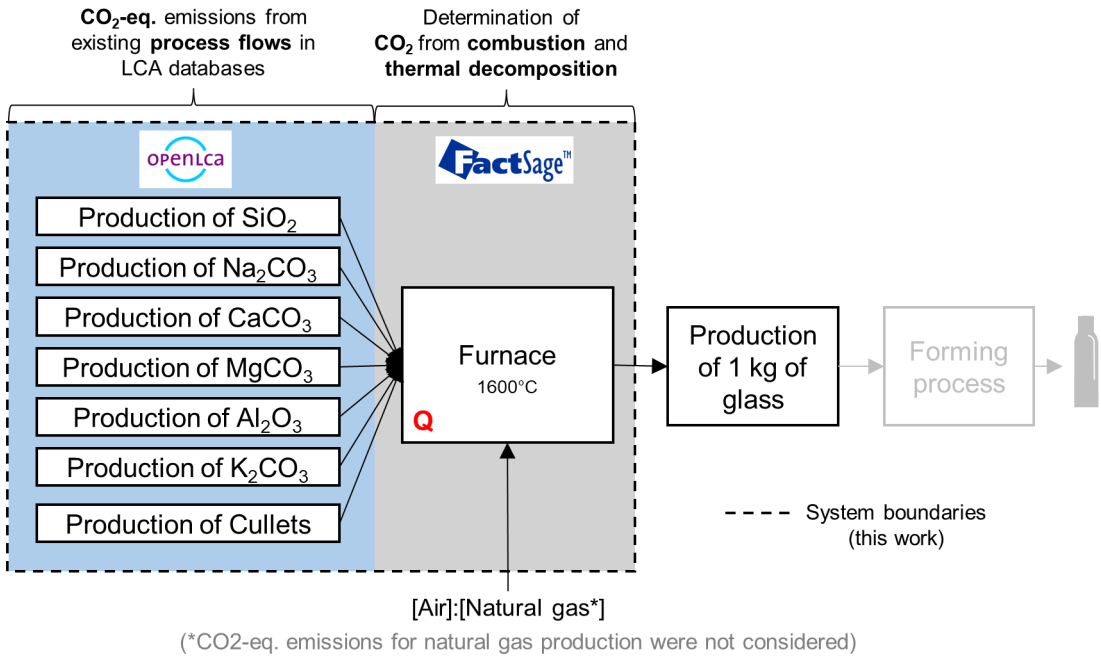

Figure 7: System boundaries for the quantification of CO_2 emissions (dashed lines) of 1kg-basis of glass produced.

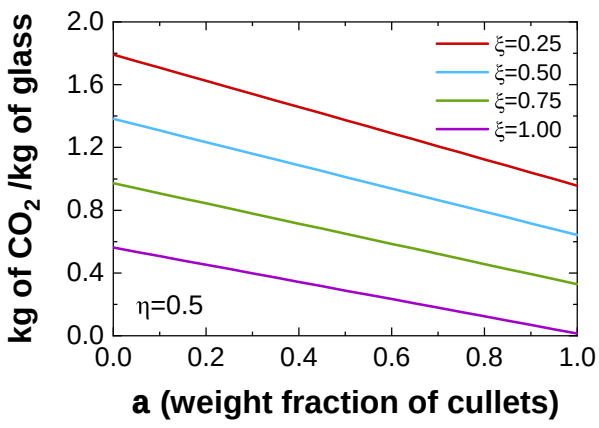

Figure 8: CO_2 emissions as a function of recycled glass (cullets) using different ratios of natural gas and renewable energies (ξ) for a furnace efficiency of η=0.5.

Table 4
Average original and normalized compositions of the uranium-thorium-and-water-free niobium leached concentrate from CBMM [76]

Component	CBMM composition wt. %	Normalized composition wt. %
Nb_2O_5	62	71.32
Fe_2O_3	5	5.75
SiO_2	0.3	0.35
BaO	2	2.30
CaO	17.5	20.13
P	0.08	0.09
S	0.03	0.03
Pb	0.03	0.03

Table 5
Original and normalized (100g-basis of Nb-concentrate) amounts of reactants fed into the aluminothermic processing of CBMM leached concentrate at 2400°C [76]

Component	CBMM amount (kg)	Normalized amount (g)
Niobium concentrate	18 000	100
Fe_2O_3	4000	22.22
Al	6000	33.33
CaF_2	750	4.17
CaO	500	2.78

well as complete Nb reduction [72, 78]. This solid mixture is then charged into a refractory-lined open steel vessel mounted on a silica sand bed lined with fluorspar and lime [76]. Magnesium turnings are used to ignite the exothermic reaction.

Table 5 shows the reactant amounts that were used in the isothermal (T = 2400 °C) equilibrium simulation of the aluminothermic process for a 100 g-basis of Nb concentrate. For this simulation, niobium oxides (NbO, NbO_2, Nb_2O_5) were merged into the slag phase (available in the FToxid database of FactSage) as an ideal solution since they are not yet fully integrated into the slag thermodynamic model. Sulfur was merged into the FTlite liquid metal as an ideal solution since Fe-S and Nb-S interactions are not fully integrated yet in this metallic liquid solution. The databases selected for this simulation are FToxid, FactPS and FTlite. For the given temperature, oxides and metals are likely to be found mainly in the molten state, thus the slag and liquid

Table 6
Partition coefficients and recoveries in metal from CBMM and FactSage aluminothermic reduction of CBMM niobium leached concentrate at 2400°C

Element	Nb	Fe	P	S	Si	Al	Pb	Ca	Ba
Partition coefficient in FactSage (slag/metal)	0.37	0.00	0.00	2041.17	0.04	14.40	0.00	92734.93	667001.70
Recovery in CBMM metal (%)	93.06	97.89	76.39	81.48	653.64	0.92	40.74	0.00	0.00
Recovery in FactSage metal (%)	72.99	99.58	99.73	0.05	96.21	6.46	57.91	0.00	0.00

metal solution model are essential for this simulation. Overall, all gas species, compounds and solutions were included in this example (refer to *equi* files in Supplementary Material). The adoption of isothermal and isobaric conditions as simplifications for modeling pyrometallurgical units is accepted in the literature [79], herein these approximations were considered for a system operating at 2400 ºC and 1 atm. For the sake of simplicity, the system was also treated as isocompositional.

The equilibrium calculation provided the partitioning coefficient between the slag and the liquid metal for each element (reported in Table 6). In this case, the partitioning coefficient is referred to as the amount of each element remaining in the slag over the amount found in the metal. It can be seen that S, Al, Ca and Ba will mostly remain in the slag, while Nb, Fe, P, Si and Pb will preferentially be transferred to the metal. According to this equilibrium calculation, 58 g of liquid metal are generated per 100 g of leached concentrated under these operating conditions. In comparison, CBMM reports collecting about 11 000 kg of ferroniobium per 18 000 kg of leached concentrate [76], which is equivalent to 61 g of metal per 100 g of leached concentrate. The comparison between unnormalized recovery in the metal from FactSage and CBMM is provided in Table 6. Recovery in metal was estimated for each element by dividing the amount collected in the metal by the amount found in the feed. According to this table, a reasonably good agreement is found except for sulfur and silicon. The silicon recovery in CBMM metal is much greater than 100%, indicating probable contamination from the lined silica sand bed upon which the feed is resting in the aluminothermic reactor [76]. As for sulfur, discrepancies are probably artifacts from the small amount found initially in the feed (0.03 wt% [76]). Note that the CBMM alloy's grade was reported as 66 wt% of Nb by [76]. In contrast, the FactSage simulation results suggest an Nb concentration of 62 wt% (red sphere in Figure 9) under the simulated conditions (*i.e.*, using the mass balance from Tables 4 and 5). Figure 9 indicates that the amount of Fe_2O_3 must be reduced from 22.22 (red sphere) to 18.5 (black diamond symbol) g/100 g of niobium-leached concentrate to achieve a grade of 66%.

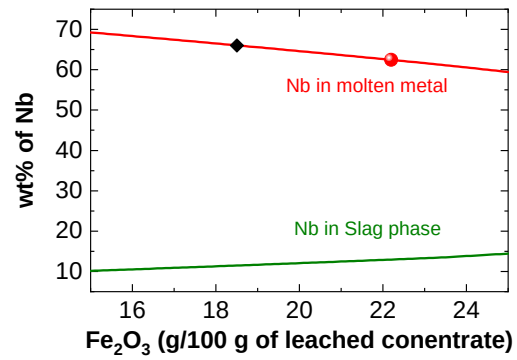

Figure 9: Effect of Fe_2O_3 additions/100 g of niobium-leached concentrate on the Nb concentration in the metallic liquid phase. The red sphere and black diamond symbols represent the theoretical Fe_2O_3 addition which is required to reach 62 and 66 %(wt.) of Nb in the liquid metallic solution respectively per 100g-basis of Nb-concentrate using the normalized composition presented in Table 5.

3.4. Case study #4: Titanium purification

In pyrometallurgical process operations, it is a common practice to add reactive chemicals (C, O_2, Cl_2, etc.) into a stream of concentrate/smelt containing impurities to facilitate the extraction of a specific metal or alloy of interest. This method explicitly relies on the chemical affinity of these reactants with specific components of the feed materials and their ability to react with impurities (or with the valuable metals) to generate new phases having distinct physicochemical properties (such as high volatility, low melting point, low density, low viscosity, etc.). This facilitates the physical separation and purification processes. Another strategy that does not involve the direct addition of reactive chemicals into a melt is by modifying the fugacity of the species that need to be separated, *i.e.* by controlling their volatilization/transfer into a gas phase. In the case of the distillation of a liquid solution, it is possible to lower the total pressure of the system to promote the transfer of the most volatile species into a gas phase or to use an inert gas to act as a carrier vector for these volatile species.

To explore the distillation process in more detail, we study here the distillation of Ti sponges produced during the reduction process of $TiCl_4$ with Mg [80], where liquid $MgCl_2$ and Mg in excess may remain in the pores. Specifically, the production of Ti sponges in the Kroll process starts from: (i) the carbo-chlorination of titanium ores to produce $TiCl_4$, followed by (ii) the reduction of $TiCl_4$ with Mg(l) producing solid Ti and $MgCl_2$(l) [81].

Advantageously, there exists a miscibility gap between Ti and Mg (Figure 10), which facilitates the separation of Mg in excess encountered after the reduction of $TiCl_4$. Because of this characteristic behavior, a distillation process

is adequate to purify Ti sponges before proceeding to the crushing step [82].

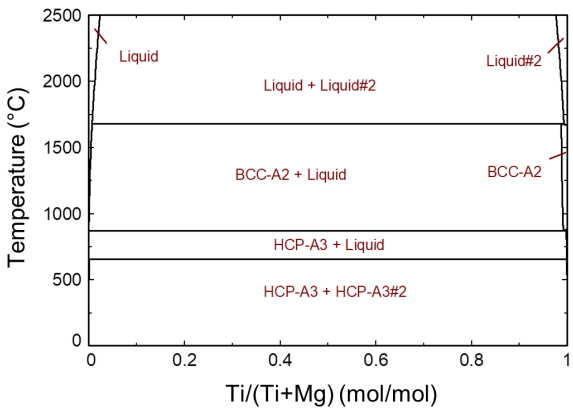

Figure 10: Mg-Ti phase diagram from FactSage documentation (FTlite database).

Argon is widely used in pyrometallurgy in order to prevent the oxidation of metallic melts and to perform degassing operations [83, 84, 85, 86]. In this section, the effect of Ar pressure on the distillation of Ti sponges contaminated with $MgCl_2$ is evaluated using equilibrium calculations. To do so, a hypothetical case where 10g of $MgCl_2$ are filling the pores of a 90g-Ti sponge was considered. The databases selected for this section are FactPS (for the gas and stoichiometric compounds) and FTlite (a specialized database for Al alloys, Mg alloys, and Ti alloys). This example can be performed by selecting only the gas and pure solid/liquid compounds, due to the immiscibility behavior of Mg and Ti (Figure 10). Additionally, the excess of Mg guarantees that all titanium-chloride species have been reduced to form the Ti sponge; hence, the formation of a $MgCl_2$-based solution containing $TiCl_2$ is avoided. Such a solution model has not been critically assessed in FactSage databases yet. However, simulations considering a $TiCl_2$-$MgCl_2$ ideal solution with an excess of Mg indicate that the titanium is preferentially transferred to the solid sponge rather than being incorporated into the $MgCl_2$-based solution. The distillation temperature was set to 1273 K since the sponge is obtained in a magnesiothermic reduction unit that operates at this temperature. For the sake of simplicity, simulations were performed under isothermal and iso-compositional conditions using the *Equilib* module of FactSage. Figure 11 shows the vacuum conditions (P_{tot}) and the associated partial pressure of argon (P_{Ar}/P_{tot}) to achieve complete volatilization of liquid $MgCl_2$. From Figure 11, it is concluded that the vacuum conditions for evaporating liquid $MgCl_2$ are less severe as a higher partial pressure of Ar is experienced in the system. By contrast, a pressure lower than 0.03 atm (*i.e.* the $MgCl_2$ vapor pressure at this operating temperature) is required to evaporate the liquid $MgCl_2$ if Ar is not considered. Ar is an inert gas which does not react with either Ti or $MgCl_2$ in this distillation unit operation. It simply modifies the equilibrium conditions to facilitate the volatilization of $MgCl_2$.

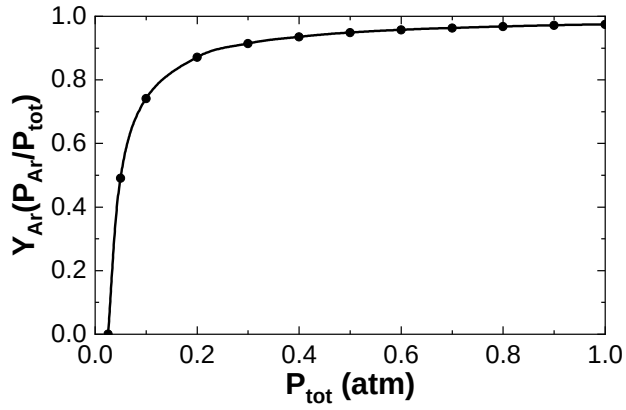

Figure 11: Evolution of the molar fraction of Ar required to completely evaporate $MgCl_2$(l), as a function of the distillation pressure in a unit operating at 1273 K.

Similarly to the investigation of $MgCl_2$ removal, a series of calculations were performed to study the removal of liquid Mg that can potentially contaminate the Ti sponges. For this scenario, an excess of 5 g of Mg (which Mg did not react with $TiCl_4$) was equilibrated with a 90g Ti-sponge in different vacuum conditions. Simulation results for the liquid Mg exposed to different system total pressures are presented in Figure 12. The addition of Ar into the gas promotes the volatilization of Mg. Note that the vacuum conditions which are required for the removal of Mg are less severe than those for $MgCl_2$ because of the substantially higher vapor pressure of Mg (0.43 atm). As such, the operating conditions for the distillation of Ti sponges are dictated by $MgCl_2$ contamination. For this operation, corrosion may arise from the potential reaction of Mg and $MgCl_2$ with the distillation vacuum system. According to Takeda *et al.* [87], these vacuum vessels are made of steel. The 316 [88] and 316L [89] stainless steels have proved good corrosion resistance under $MgCl_2$ environments.

4. Conclusion

To illustrate the strength of computational thermochemistry, high-temperature process simulations were carried out. Simulations were performed using FactSage, a metallurgy-specialized thermochemical package. Four case studies were investigated to illustrate the importance of fundamental thermodynamic concepts for engineers-in-training. The examples explored were:

1. **Carbo-reduction:** This section illustrates the importance of Gibbs free energy and its implications leading to the construction of the Ellingham diagram, which is a traditional reference for the design of pyrometallurgical processes. Additionally, the limitations of this traditional approach compared to CT packages

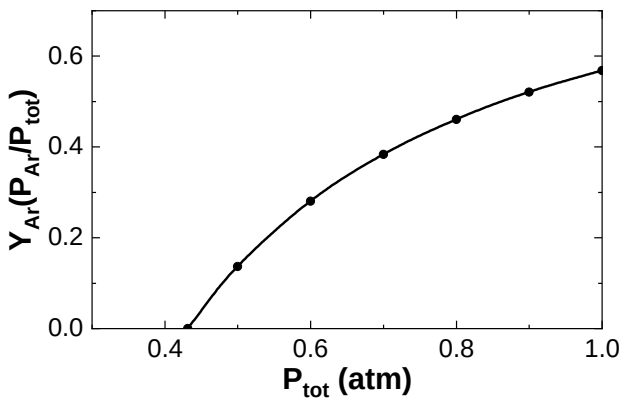

Figure 12: Evolution of the molar fraction of Ar required to completely evaporate Mg(l), as a function of the distillation pressure in a unit operating at 1273 K.

were discussed (*e.g.*, prediction of multi-phasic system/secondary reactions). An example of the FactSage simulation capabilities is presented through the carbo-reduction of roasted nickel sulfide ores, which is devoted to the production of a ferronickel alloy.

2. **Energy and mass balances for glass production and recycling:** A model to forecast the CO_2 emissions for glass production was proposed. It incorporates the mass and energy balance results from CT calculations and the raw materials footprint index from Life-Cycle Assessment (LCA) databases. This model considers the effect of glass recycling, as well as the efficiency of the melting furnace. This approach can be extended to other manufacturing processes to quantify carbon emissions.
3. **Aluminothermic reactor to produce niobium:** This example exhibits the implication of the partitioning coefficients involving the equilibrium between several liquid solutions. More precisely, those parameters were calculated for the production of a ferroniobium alloy considering the leached concentrate composition reported by the CBMM mining company. Additionally, the metal recovery estimations from the thermochemical simulations were consistent with those reported by CBMM, showing the reliability of using CT packages for complex multi-phasic systems.
4. **Titanium purification:** In this section, the purification of Ti-sponges obtained from carbo-chlorination (Kroll process) was investigated. The effect of adding Ar to the system to volatilize liquid impurities ($MgCl_2$ and Mg) is also exemplified. It was shown that the vacuum conditions are more severe for $MgCl_2$ than Mg. This example illustrates how engineers can benefit from thermodynamic concepts (fugacity) to modulate the volatilization of undesired species.

In conclusion, it is demonstrated that CT is a powerful tool for high-temperature process design. Thus, engineers can profit from this resource to understand the behavior of matter, predict and prevent process failures, develop new materials, optimize energy usage, and design cleaner transformation processes. Remarkably, it was shown that CT can be coupled to LCA to quantify the greenhouse gas emissions to manufacture specific products. This approach is particularly convenient for designing new operations or incorporating consistent theoretical-based data for non-existent process flows in LCA packages.

Acknowledgements

We acknowledge the support of the Natural Sciences and Engineering Research Council of Canada (NSERC) *via* the Discovery Grant of Prof. Harvey (RGPIN-2017-06168).

Declaration of competing interest

The authors declare that they have no known competing financial interests or personal relationships that could have appeared to influence the work reported in this paper.

Data availability

The Factsage *Equilib* files (.equi) required to reproduce the simulations of this work are provided in the Electronic Supplementary Material (ESM).

References

[1] M. Athar, A. Mohd Shariff, A. Buang, M. Shuaib Shaikh, M. Ishaq Khan, Review of process industry accidents analysis towards safety system improvement and sustainable process design, Chemical Engineering & Technology 42 (2019) 524–538.

[2] Y. Meng, Y. Yang, H. Chung, P.-H. Lee, C. Shao, Enhancing sustainability and energy efficiency in smart factories: A review, Sustainability 10 (2018) 4779.

[3] K. Ejsmont, B. Gladysz, A. Kluczek, Impact of industry 4.0 on sustainability—bibliometric literature review, Sustainability 12 (2020) 5650.

[4] J. García-Serna, L. Pérez-Barrigón, M. Cocero, New trends for design towards sustainability in chemical engineering: Green engineering, Chemical Engineering Journal 133 (2007) 7–30.

[5] A. Nikolopoulou, M. G. Ierapetritou, Optimal design of sustainable chemical processes and supply chains: A review, Computers & Chemical Engineering 44 (2012) 94–103.

[6] M. A. Curran, Life cycle assessment: a review of the methodology and its application to sustainability, Current Opinion in Chemical Engineering 2 (2013) 273–277.

[7] J.-P. Harvey, W. Courchesne, M. D. Vo, K. Oishi, C. Robelin, U. Mahue, P. Leclerc, A. Al-Haiek, Greener reactants, renewable energies and environmental impact mitigation strategies in pyrometallurgical processes: A review, MRS Energy & Sustainability (2022) 1–36.

[8] A. Vai, J. Yurko, D. Wang, D. Sadoway, Molten oxide electrolysis for lunar oxygen generation using in situ resources, 2010.

[9] J. Wiencke, H. Lavelaine, P.-J. Panteix, C. Petitjean, C. Rapin, Electrolysis of iron in a molten oxide electrolyte, Journal of Applied Electrochemistry 48 (2018) 115–126.

[10] T. Nguyen, Z. Abdin, T. Holm, W. Mérida, Grid-connected hydrogen production via large-scale water electrolysis, Energy conversion and Management 200 (2019) 112108.

[11] S. S. Kumar, V. Himabindu, Hydrogen production by pem water electrolysis–a review, Materials Science for Energy Technologies 2 (2019) 442–454.

[12] H. A. Miller, K. Bouzek, J. Hnat, S. Loos, C. I. Bernäcker, T. Weißgärber, L. Röntzsch, J. Meier-Haack, Green hydrogen from anion exchange membrane water electrolysis: a review of recent developments in critical materials and operating conditions, Sustainable Energy & Fuels 4 (2020) 2114–2133.

[13] J. Tang, M.-s. Chu, F. Li, C. Feng, Z.-g. Liu, Y.-s. Zhou, Development and progress on hydrogen metallurgy, International Journal of Minerals, Metallurgy and Materials 27 (2020) 713–723.

[14] K. Su, X. Ma, J. Parianos, B. Zhao, Thermodynamic and experimental study on efficient extraction of valuable metals from polymetallic nodules, Minerals 10 (2020) 360.

[15] M. Atsushi, H. Uemura, T. Sakaguchi, Midrex processes, Kobelco Technology Review 29 (2010) 50–57.

[16] B. Delacroix, J. Rastoueix, L. Fradette, F. Bertrand, B. Blais, Cfd-dem simulations of solid-liquid flow in stirred tanks using a non-inertial frame of reference, Chemical Engineering Science 230 (2021) 116137.

[17] D.-H. Kim, T. J. Kim, X. Wang, M. Kim, Y.-J. Quan, J. W. Oh, S.-H. Min, H. Kim, B. Bhandari, I. Yang, et al., Smart machining process using machine learning: A review and perspective on machining industry, International Journal of Precision Engineering and Manufacturing-Green Technology 5 (2018) 555–568.

[18] D. Weichert, P. Link, A. Stoll, S. Rüping, S. Ihlenfeldt, S. Wrobel, A review of machine learning for the optimization of production processes, The International Journal of Advanced Manufacturing Technology 104 (2019) 1889–1902.

[19] A. Angelopoulos, E. T. Michailidis, N. Nomikos, P. Trakadas, A. Hatziefremidis, S. Voliotis, T. Zahariadis, Tackling faults in the industry 4.0 era—a survey of machine-learning solutions and key aspects, Sensors 20 (2020) 109.

[20] A. Dogan, D. Birant, Machine learning and data mining in manufacturing, Expert Systems with Applications (2020) 114060.

[21] J.-P. Harvey, F. Lebreux-Desilets, J. Marchand, K. Oishi, A.-F. Bouarab, C. Robelin, A. E. Gheribi, A. D. Pelton, On the application of the factsage thermochemical software and databases in materials science and pyrometallurgy, Processes 8 (2020).

[22] K. Hack, Computational thermodynamics: A mature scientific tool for industry and academia, Pure and Applied Chemistry 83 (2011) 1031–1044.

[23] E. Jak, Modelling metallurgical furnaces—making the most of modern research and development techniques, in: Extraction 2018: Proceedings of the First Global Conference on Extractive Metallurgy, Springer, 2018, pp. 103–125.

[24] N. Huda, J. Naser, G. Brooks, M. A. Reuter, R. W. Matusewicz, Computational fluid dynamic modeling of zinc slag fuming process in top-submerged lance smelting furnace, Metallurgical and Materials Transactions B 43 (2012) 39–55.

[25] J. Rezende, R. van Schalkwyk, M. Reuter, M. to Baben, A dynamic thermochemistry-based process model for lead smelting in the tsl process, Journal of Sustainable Metallurgy 7 (2021) 964–977.

[26] P. Taskinen, A. Jokilaakso, D. Lindberg, J. Xia, Modelling copper smelting–the flash smelting plant, process and equipment, Mineral Processing and Extractive Metallurgy 129 (2020) 207–220.

[27] C. Bale, E. Bélisle, P. Chartrand, S. Decterov, G. Eriksson, A. Gheribi, K. Hack, I.-H. Jung, Y.-B. Kang, J. Melançon, A. Pelton, S. Petersen, C. Robelin, J. Sangster, P. Spencer, M.-A. Van Ende, Factsage thermochemical software and databases, 2010–2016, Calphad 54 (2016) 35–53.

[28] A. D. Pelton, Phase diagrams and thermodynamic modeling of solutions, Academic Press, 2018.

[29] N. Saunders, A. P. Miodownik, CALPHAD (calculation of phase diagrams): a comprehensive guide, Elsevier, 1998.

[30] H. Lukas, S. Fries, B. Sundman, Computational Thermodynamics: The Calphad Method, Cambridge University Press, 2007. URL: https://books.google.ca/books?id=PALgAAAAMAAJ.

[31] J.-P. Harvey, G. Eriksson, D. Orban, P. Chartrand, Global minimization of the gibbs energy of multicomponent systems involving the presence of order/disorder phase transitions, American Journal of Science 313 (2013) 199–241.

[32] C. W. Bale, E. Bélisle, P. Chartrand, S. Decterov, G. Eriksson, A. Gheribi, K. Hack, I.-H. Jung, Y.-B. Kang, J. Melançon, et al., Reprint of: Factsage thermochemical software and databases, 2010–2016, Calphad 55 (2016) 1–19.

[33] G. ERIKSON, Thermodynamic studies of high temperature equilibria. xii. solgasmi x, a computer program for calculation of equilibrium compositions in multiphase systems (1975).

[34] G. Eriksson, K. Hack, Calculation of phase equilibria in multicomponent alloy systems using a specially adapted version of the program 'solgasmix', Calphad 8 (1984) 15–24.

[35] W. Thompson, A. Pelton, C. Bale, Extension to solgasmix for interactive calculations with the f* a* c* 7t thermodynamic database, Calphad 7 (1983) 113–123.

[36] W. Thompson, G. Eriksson, A. Pelton, C. Bale, Heterogeneous equilibrium calculations with multicomponent solution models-solgasmix and the f* a* c* t system, in: Proceedings of the International Symposium on Computer Software in Chemical and Extractive Metallurgy, Elsevier, 1989, pp. 87–106.

[37] F. Habashi, Alloys: preparation, properties, applications, John Wiley & Sons, 2008.

[38] J.-P. Harvey, M. Khalil, J. Chaouki, Pyrometallurgical Processes for Recycling Waste Electrical and Electronic Equipment, John Wiley & Sons, Ltd, 2022, pp. 135–164. doi:https://doi.org/10.1002/9783527816392.ch7.

[39] A. Akcil, Y. A. Ibrahim, P. Meshram, S. Panda, Abhilash, Hydrometallurgical recycling strategies for recovery of rare earth elements from consumer electronic scraps: a review, Journal of Chemical Technology & Biotechnology (2021).

[40] U. K. Mudali, M. Patil, R. Saravanabhavan, V. Saraswat, Review on e-waste recycling: Part ii—technologies for recovery of rare earth metals, Transactions of the Indian National Academy of Engineering (2021) 1–19.

[41] U. K. Mudali, M. Patil, R. Saravanabhavan, V. Saraswat, Review on e-waste recycling: Part i—a prospective urban mining opportunity and challenges, Transactions of the Indian National Academy of Engineering (2021) 1–22.

[42] S. M. Abdelbasir, S. S. Hassan, A. H. Kamel, R. S. El-Nasr, Status of electronic waste recycling techniques: a review, Environmental Science and Pollution Research 25 (2018) 16533–16547.

[43] H.-Y. Kang, J. M. Schoenung, Electronic waste recycling: A review of us infrastructure and technology options, Resources, Conservation and Recycling 45 (2005) 368–400.

[44] R. Ahirwar, A. K. Tripathi, E-waste management: A review of recycling process, environmental and occupational health hazards, and potential solutions, Environmental Nanotechnology, Monitoring & Management 15 (2021) 100409.

[45] S. M. Abdelbasir, C. T. El-Sheltawy, D. M. Abdo, Green processes for electronic waste recycling: a review, Journal of Sustainable Metallurgy 4 (2018) 295–311.

[46] M. Khalil, J. Chaouki, J.-P. Harvey, On the investigation of the thermal degradation of waste printed circuit boards for recycling applications, Advanced Sustainable Systems (2021) 2100054.

[47] A. Saba, A. Elsherief, Continuous electrowinning of zinc, Hydrometallurgy 54 (2000) 91–106.

[48] T. P. Battle, J. P. Downey, L. D. May, B. R. Davis, N. R. Neelameggham, S. Sanchez-Segado, P. C. Pistorius, et al., Drying, roasting, and calcining of minerals, John Wiley & Sons, 2015.

[49] F. Habashi, Principles of Extractive Metallurgy: Pyrometallurgy, Routledge, 2017.

[50] J. E. Olsen, Q. G. Reynolds, Mathematical modeling of furnace drainage while tapping slag and metal through a single tap-hole, Metallurgical and Materials Transactions B 51 (2020) 1750–1759.

[51] B. Hübschen, J. G. Krüger, N. J. Keegan, W. Schneider, Fundamental research about liquid metal filtration, Continuous Casting (2000) 20–25.

[52] H. J. T. Ellingham, Reducibility of oxides and sulphides in metallurgical processes, Journal of the Society of Chemical Industry 63

(1944) 125–133.

[53] M. Hasegawa, Ellingham diagram, in: Treatise on Process Metallurgy, Elsevier, 2014, pp. 507–516.

[54] R. Loison, P. Foch, A. Boyer, Coke: quality and production, Elsevier, 2014.

[55] R. H. Eric, Chapter 1.10 - production of ferroalloys, in: S. Seetharaman (Ed.), Treatise on Process Metallurgy, Elsevier, Boston, 2014, pp. 477–532. URL: https://www.sciencedirect.com/science/article/pii/B9780080969886000055. doi:https://doi.org/10.1016/B978-0-08-096988-6.00005-5.

[56] A. Warner, C. Diaz, A. Dalvi, P. Mackey, A. Tarasov, Jom world nonferrous smelter survey, part iii: Nickel: Laterite, Jom 58 (2006) 11–20.

[57] C. Diaz, C. Landolt, A. Vahed, A. Warner, J. Taylor, A review of nickel pyrometallurgical operations, JOM 40 (1988) 28–33.

[58] M. S. Moats, W. G. Davenport, Nickel and cobalt production, in: Treatise on Process Metallurgy, Elsevier, 2014, pp. 625–669.

[59] G. C. Wang, 3 - nonferrous metal extraction and nonferrous slags, in: G. C. Wang (Ed.), The Utilization of Slag in Civil Infrastructure Construction, Woodhead Publishing, 2016, pp. 35–61. URL: https://www.sciencedirect.com/science/article/pii/B9780081003817000033. doi:https://doi.org/10.1016/B978-0-08-100381-7.00003-3.

[60] F. Crundwell, M. Moats, V. Ramachandran, T. Robinson, W. Davenport, Smelting of Laterite Ores to Ferronickel, 2011, pp. 67–83. doi:10.1016/B978-0-08-096809-4.10006-1.

[61] C. Sagadin, S. Luidold, C. Wagner, C. Wenzl, Melting behaviour of ferronickel slags, Jom 68 (2016) 3022–3028.

[62] R. A. Schaut, W. P. Weeks, Historical review of glasses used for parenteral packaging, PDA journal of pharmaceutical science and technology 71 (2017) 279–296.

[63] M. Kovačec, A. Pilipović, N. Štefanić, Improving the quality of glass containers production with plunger process control, CIRP Journal of Manufacturing Science and Technology 3 (2010) 304–310.

[64] J. D. Musgraves, J. Hu, L. Calvez, Springer handbook of glass, Part A, Springer, 2019.

[65] R. Frischknecht, N. Jungbluth, H.-J. Althaus, G. Doka, R. Dones, T. Heck, S. Hellweg, R. Hischier, T. Nemecek, G. Rebitzer, et al., The ecoinvent database: overview and methodological framework (7 pp), The international journal of life cycle assessment 10 (2005) 3–9.

[66] F.-F. Li, S. Liu, B. Cui, J. Lau, J. Stuart, B. Wang, S. Licht, A one-pot synthesis of hydrogen and carbon fuels from water and carbon dioxide, Advanced Energy Materials 5 (2015) 1401791.

[67] K. Motzfeldt, The thermal decomposition. of sodium carbonate by the effusion method, The Journal of Physical Chemistry 59 (1955) 139–147.

[68] Y. Mandal, P. K. Sinha, A. K. Mandal, Effect of melting time on volatility, oh in glass in microwave processing, Materials and Manufacturing Processes 36 (2021) 426–434.

[69] Z. Wang, T. Maotsela, P. M. Toperesu, G. M. Kale, J. Daji, D. Parkinson, Dynamic and static corrosion of alpha-alumina bonded refractory in contact with molten soda-lime-silica (sls) glass, Ceramics International 45 (2019) 725–732.

[70] R. G. C. Beerkens, J. van Limpt, Energy Efficiency Benchmarking of Glass Furnaces, John Wiley & Sons, Ltd, 2002, pp. 93–105. doi:https://doi.org/10.1002/9780470294727.ch7.

[71] M. Kato, The production of ultrahigh-purity copper for advanced applications, Jom 47 (1995) 44–46.

[72] C. de Faria Sousa, The evolution of fenb manufacturing, in: International Symposium on Niobium 2001, 2001.

[73] S. Albrecht, C. Cymorek, J. Eckert, Niobium and Niobium Compounds, American Cancer Society, 2011. doi:https://doi.org/10.1002/14356007.a17_251.pub2.

[74] J. Tremblay, L. Bédard, G. Matton, A petrographic study of nb-bearing minerals at the saint-honoré niobium deposit, in: Symposium on critical and strategic materials. British Columbia Geological Survey Paper, volume 3, 2015, p. 75.

[75] A. Filho, B. F. Riffel, C. Sousa, Some aspects of the mineralogy of cbmm niobium deposit and mining and pyrochlore ore processing-araxa, mg- brazil., in: International Symposium on Niobium 2001, 2001, pp. 53–65.

[76] O. d. S. P. Fo, R. de Fuccio Jr, E. Betz, Mining, ore preparation and niobium-based materials production at araxá, brazil, High Temperature Materials and Processes 11 (1993) 119–138.

[77] Tantalum-Niobium-International-Study-Center, T.i.c. bullatin no.107, 2001. URL: https://www.tanb.org/images/Bulletin107.pdf.

[78] J. Yang, F. Bourgeois, K. Bru, A. Hakkinen, E. Andreiadis, D. Meyer, Q. Bellier, H. BArt, S. Virolainen, J. Lambert, et al., State of the art on the recovery of refractory metals from primary resources, msp-reframe, european union's horizon 2020 research & innovation programme under grant agreement no. 688993, accessed march 20 th, 2020, 2016.

[79] C. Pickles, Thermodynamic modelling of the multiphase pyrometallurgical processing of electric arc furnace dust, Minerals Engineering 22 (2009) 977–985.

[80] R. Subramanyam, Some recent innovations in the kroll process of titanium sponge production, Bulletin of Materials Science 16 (1993) 433–451.

[81] Y. Xia, H. D. Lefler, Z. Z. Fang, Y. Zhang, P. Sun, Energy consumption of the kroll and hamr processes for titanium production, in: Extractive Metallurgy of Titanium, Elsevier, 2020, pp. 389–410.

[82] D. Fray, Novel methods for the production of titanium, International Materials Reviews 53 (2008) 317–325.

[83] H. Jalkanen, L. Holappa, Chapter 1.4 - converter steelmaking, in: S. Seetharaman (Ed.), Treatise on Process Metallurgy, Elsevier, Boston, 2014, pp. 223–270. URL: https://www.sciencedirect.com/science/article/pii/B9780080969886000146. doi:https://doi.org/10.1016/B978-0-08-096988-6.00014-6.

[84] G. Kashakashvili, I. Kashakashvili, O. S. Mikadze, Steel smelting in an improved ladle-furnace unit, Steel in Translation 43 (2013) 436–440.

[85] N. Zakharov, F. Nedopekin, A. Trotsan, P. Kharlashin, Mathematical simulation of mass-transfer processes in off-furnace degassing of metal by floating inert gas bubbles, Journal of Engineering Physics and Thermophysics 78 (2005) 482–486.

[86] M. G. Dumitru, A. Ioana, N. Constantin, F. Ciobanu, M. Pollifroni, Steel refining possibilities in lf, IOP Conference Series: Materials Science and Engineering 294 (2018) 012018.

[87] O. Takeda, T. Ouchi, T. H. Okabe, Recent progress in titanium extraction and recycling, Metallurgical and Materials Transactions B 51 (2020) 1315–1328.

[88] L. Guo, Q. Liu, H. Yin, T. Pan, Z. Tang, Excellent corrosion resistance of 316 stainless steel in purified nacl-mgcl2 eutectic salt at high temperature, Corrosion Science 166 (2020) 108473.

[89] S. Santa-Aho, M. Kiviluoma, T. Jokiaho, T. Gundgire, M. Honkanen, M. Lindgren, M. Vippola, Additive manufactured 316l stainless-steel samples: Microstructure, residual stress and corrosion characteristics after post-processing, Metals 11 (2021) 182.

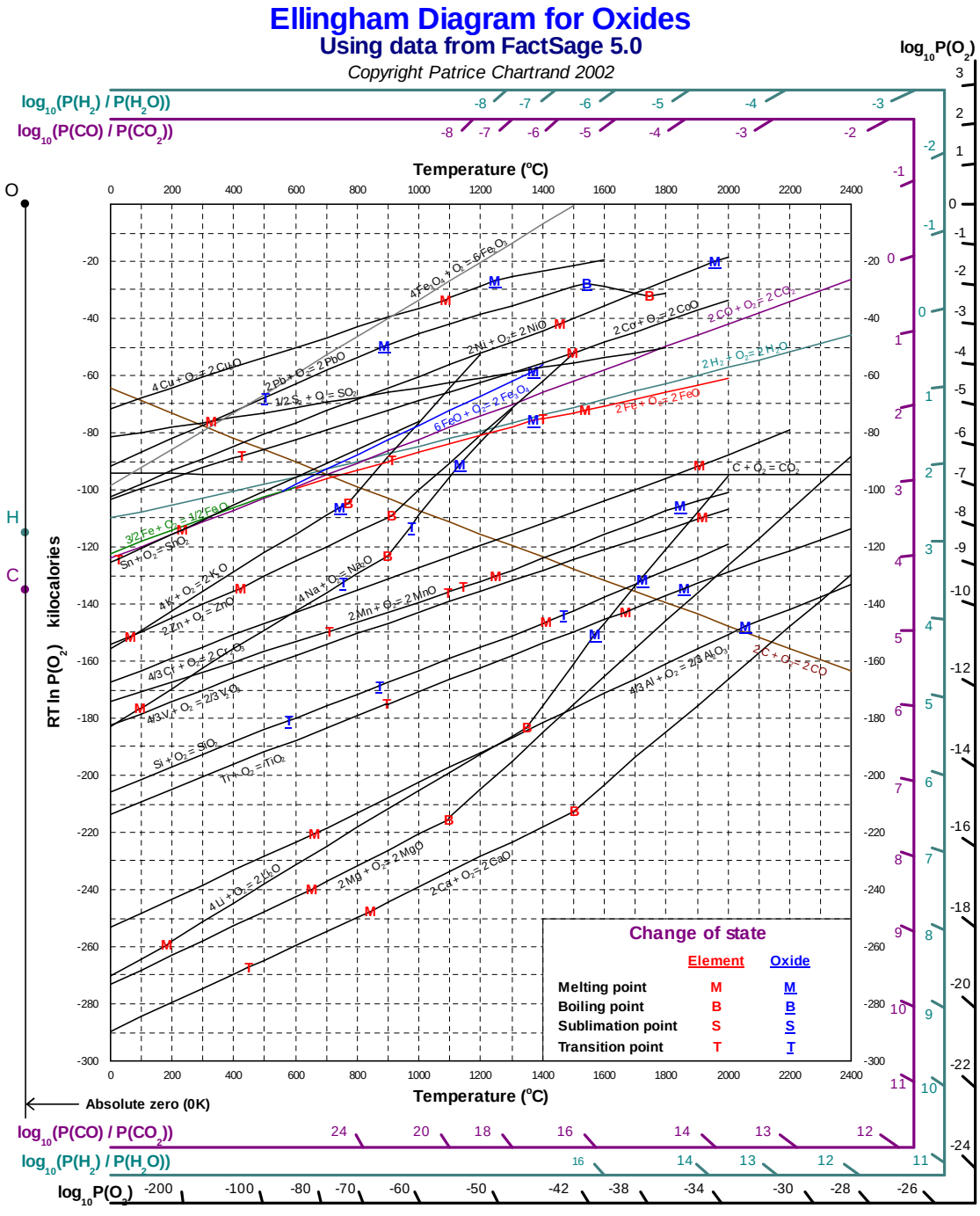

Figure A.1: Ellingham diagram.

Appendix